Journal of chemical & engineering data

Article

pubs.acs.org/jced

# Using Molecular Simulations To Develop Reliable Design Tools and Correlations for Engineering Applications of Aqueous Electrolyte Solutions

Kevin R. Hinkle,[†] Cynthia J. Jameson,[‡] and Sohail Murad*[,§]

[†]Department of Chemical Engineering, and [‡]Department of Chemistry, University of Illinois at Chicago, Chicago, Illinois 60607, United States

[§]Department of Chemical and Biological Engineering, Illinois Institute of Technology, Chicago, Illinois 60616, United States

Supporting Information

**ABSTRACT:** Many industrial processes involve processing aqueous electrolyte solutions. There is thus a need for accurate theories to predict their thermophysical properties. Recent studies have shown that the size of the hydrated ion plays an important role in determining these properties. In this study, we first used molecular dynamics simulations to estimate the effective hydrated ionic size and the free energy of solvation, and then developed correlations allowing for the prediction of these quantities. The temperature dependence of these solution properties was also investigated. Our studies have shown that the effective (hydrated) size, the charge density, and the free energy of solvation of the ions are strongly interdependent. The effective hydrated ionic size also plays an important role in determining the selectivity of membranes to remove such hydrated ions from solutions, for example, in membrane based desalination processes, and related water purification technologies.

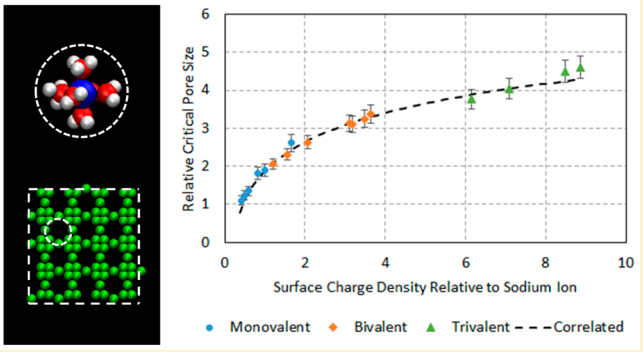


## INTRODUCTION

Aqueous electrolyte solutions play an important role in a wide range of industrial processes that include gas/wastewater treatment; separations via crystallization, distillation, and various membrane technologies; the production of energy (as in electrolytic batteries); and electrodeposition. These solutions are also responsible for many undesirable consequences such as corrosion. Aqueous electrolyte solutions are used in these processes in a variety of chemical compositions (solutes), concentrations, and system conditions. While the molecular properties of water are somewhat better understood, the addition of ions greatly affects both thermodynamic and transport behavior. The prediction of these properties—especially at high concentrations which exhibit highly nonideal behavior—is a rather difficult challenge that must be addressed during the design of industrial processes involving these materials. Many theoretical, semiempirical, and empirical models have been proposed to address these needs and reports by Zematis et al.,[1] Pitzer,[2] Rafal et al.,[3] Loehe and Donohue,[4] and Anderko et al.[5] provide a detailed picture of the thermodynamics of aqueous electrolyte systems at industrially relevant conditions. Of particular interest is a modified nonrandom two liquid (NRTL) approach proposed by Chen et al.[6] that accounts for the electrolytic species as hydrated complexes rather than simple ions for the purpose of estimating activity coefficients. The success of this method along with an earlier computational study by Paritosh and Murad[7] suggests that simple electrolytes do not behave as ions surrounded by bulk water, but as multiatomic complexes consisting of the ion and several water molecules loosely bound by Coulombic forces. These clusters of ions and water influence a wide range of thermophysical and transport properties such as viscosity, electrical/thermal conductivity, and diffusivity. They especially have a significant impact on the selectivity and flux rates achieved when using membrane-based technologies for separation, which will be the main focus of this report.

Selectively permeable membranes are used for many applications such as gas separation,[8−11] desalination,[12−15] dialysis,[16−18] batteries,[19−21] biosensing,[22] and drug delivery.[23−25] Therefore, the efficient design of membranes requires a deep and thorough understanding of the membrane interactions with aqueous electrolyte solutions which are crucial for the success of many separation processes. The morphology and functionality of semipermeable membranes allow for the passage of certain chemical species while at the same time blocking others from passing through the system. Many engineered membranes that are in use today operate on the basis of molecular sieving (steric operations) for the desired

**Received:** November 9, 2015
**Accepted:** February 24, 2016
**Published:** March 8, 2016





DOI: 10.1021/acs.jced.5b00945
J. Chem. Eng. Data 2016, 61, 1578−1584

selectivity; that is to say, they operate by separating various species on account of their size. The desired flux is often determined by Coulombic forces that then facilitate the movement of the desired species within the membrane. The first synthetic membrane of this type was developed in the 1960s by Loeb and Sourirajan.[12] These membranes contain pores of a size such that larger molecular species cannot pass through while still allowing for the transport of smaller molecules. Depending on the system of interest and which materials must be blocked from passage through the membrane, the pore size is selected to achieve the necessary separation. This selection assumes that the relative sizes of the species to be separated are known, but this is not always the case. As discussed previously, the effective size of ionic species in aqueous solution is greater than that of the bare ion due to the presence of a surrounding hydration layer. Depending on the free energy of solvation, this hydration layer can be loosely or tightly bound and this can also greatly influence the transport of the ionic species through porous materials. This is because a hydration shell that is not rigid (primarily due to lower free energies of solvation) has the flexibility to then squeeze into smaller pores, which a rigidly held hydration would not succeed in entering. For example in a previous study[26] we found that potassium ions, which are larger than sodium ions, were able to permeate a carbon nanotube while sodium could not because the hydration shell of the potassium ions was not as rigidly held. This study aims to use molecular dynamics simulations to further examine this phenomenon and provide guidance to engineers regarding the two contributing factors: effective size of electrolytes in aqueous solution, and their free energy of solvation in the design of more efficient membranes. These predictions can then be used to help reduce the experimental trials needed in designing new membrane-based separation processes involving aqueous electrolyte solutions, as well as for developing new methods to predict thermophysical properties of such solutions.

## COMPUTATIONAL METHODS

**System Setup.** This molecular dynamics study utilizes a system setup developed previously to determine the selectivity of zeolite membranes to solvated ions;[27] therefore, it is only discussed briefly here. As seen in Figure 1a, two membranes are used along with periodic boundary conditions in all dimensions to create two separate solution/solvent compartments in one dimension, while the system can be considered infinite in the other two dimensions.

The model membranes in this study consist of a single atomic layer of silicon atoms arranged in an array of eight-membered rings (Figure 1b,c). Systems with ring sizes of either 5.7 or 8 Å were used, and by adjusting the size of these ring atoms a range of pore sizes (from 3.4 to7.0 Å in increments of 0.1 Å) were prepared. One compartment consisted of pure water while the other contained an ionic solution of 5 mol % for the various mono- and bivalent salts or 3 mol % for the trivalent salts. Our previous studies have shown that at these concentrations very few ion pairs are observed,[28] which do not affect the results. The cations examined include five monovalent alkali ions ($Li^+$, $Na^+$, $K^+$, $Rb^+$, $Cs^+$), four bivalent alkaline earth ions ($Mg^{2+}$, $Ca^{2+}$, $Sr^{2+}$, $Ba^{2+}$), and eight ions from various groups ($Ag^+$, $V^{2+}$, $Fe^{2+}$, $Zn^{2+}$, $Al^{3+}$, $Ti^{3+}$, $Fe^{3+}$, $Cr^{3+}$). The chloride ion ($Cl^-$) was used as the counterion in all cases. The number of solvent molecules and the size of the solution compartment was adjusted in order to achieve the correct solution densities in the various systems. Densities for LiCl, KCl, NaCl, $MgCl_2$, $CaCl_2$, $SrCl_2$, $BaCl_2$, $ZnCl_2$, $FeCl_2$, $AlCl_3$, $CrCl_3$, and $FeCl_3$ solutions were found at various system conditions using the correlation developed by Laliberté and Cooper.[29] The remaining densities were estimated using species from the same valence family. All atom counts and system/compartment sizes are tabulated in the Supporting Information. All membrane atoms were tethered to their initial positions using a simple harmonic potential. Short-range site−site interaction potentials used the extended Lennard-Jones (LJ) potential of the form:

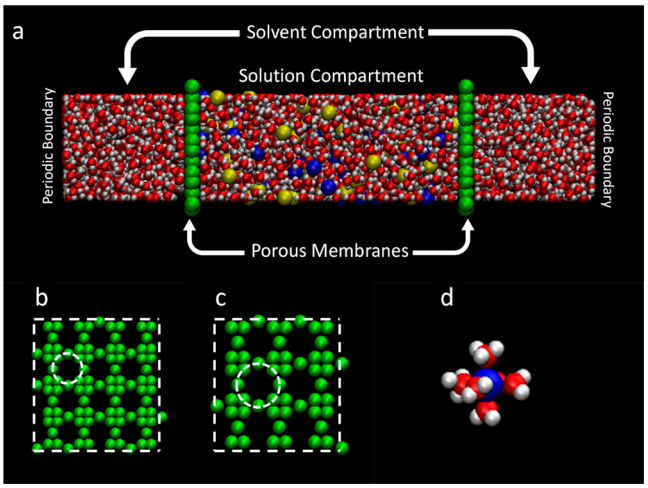


**Figure 1.** (a) System schematic showing alternating solution/solvent compartments; membranes with ring size of (b) 5.7 Å and (c) 8 Å; (d) illustration of how the hydration shell contributes to the effective ionic radius.

$$U_{ij} = 4\varepsilon_{ij}\left[\left(\frac{\sigma_{ij}}{r_{ij}}\right)^{12} - \left(\frac{\sigma_{ij}}{r_{ij}}\right)^{6}\right] + C\frac{q_i q_j}{r_{ij}}; \quad r_{ij} < r_c \tag{1}$$

where $r_{ij}$ is the distance between sites $i$ and $j$, $r_c$ is the cutoff radius (10 Å) beyond which the short-range interactions are neglected, $\sigma_{ij}$ and $\varepsilon_{ij}$ are the LJ parameters, and $q_i$ and $q_j$ are the atomic charges on sites $i$ and $j$, respectively. Long range electrostatics (beyond the cutoff of 10 Å) were computed using the particle-mesh Ewald scheme (PME) with an accuracy of $10^{-4}$. These potentials were summed over all sites to obtain the total intermolecular interactions. The common SPC/E model was used for water[30] while the models for the various ions were taken from a number of previously published studies: Joung et al.[31] for monovalent ions in Group I; Mamatkulov et al.[32] for bivalent ions in Group II; DuBois et al.[33] for $Ag^+$; Aguilar et al.[34] for $Fe^{2+}$; Ansari et al.[35] for $Zn^{2+}$; Li et al.[36] for $V^{2+}$; Faro et al.[37] for $Al^{3+}$; and Won[38] for $Ti^{3+}$, $Fe^{3+}$, and $Cr^{3+}$ (see Supporting Information for parameter tabulation). The membrane atoms are uncharged and their LJ size parameter, $\sigma_{mem}$, was varied (from 1.0 to2.5 Å) in order to fine-tune the pore size and determine at which value the membrane became impermeable to each cation. The pore diameter, $d_{pore}$, is defined in eq 2 where $d_{c\text{-}c}$ denotes the center-to-center distance of the membrane atoms across the eight-membered ring.

$$d_{pore} = d_{c-c} - \sigma_{mem} \tag{2}$$

**Simulation Details.** The open source software package Packmol[39] was used to construct the initial nonoverlapping



DOI: 10.1021/acs.jced.5b00945
J. Chem. Eng. Data 2016, 61, 1578−1584

random solute/solvent configurations. All simulations exist at nonequilibrium conditions and were run using the LAMMPS simulation package.[40] Energy minimization was performed using the Polak-Ribiere conjugate gradient method and the Verlet algorithm was used to carry out the time integration. The system volume was kept unchanged and a Nosé−Hoover thermostat (with a damping constant of 100 fs) was applied to the solution and membrane atoms throughout the simulation in order to maintain a constant temperature of 298 K. Following minimization, a time step of 1.0 fs was used for production runs of 5 000 000 steps (5 ns).

## RESULTS AND DISCUSSION

**Model Verification.** The existence of the hydration shell surrounding an ion results in its effective size in aqueous solution being larger than the ionic radius (Figure 1d); therefore, the hydration shell of each ion was examined and compared with experimental values in order to ensure that the models utilized display the correct behavior in bulk solution. The ion−water radial distribution function (RDF) was found for each ion in solution by defining the position of the water molecule to be that of the oxygen atom. The distance of the first peak from the origin represents this average ion−oxygen distance, $d_{I-O}$, for the first hydration shell. The uncertainty of the location of this peak can be estimated by the size of the radial bins used when calculating the RDF. Values found in this analysis are compared (Table 1) with experimental neutron and

**Table 1. Cation−Water Distance within the First Hydration Shell of the Simulated Ions**

| | $d_{I-O}$, Å | |
|---|---|---|
| ion | this work | Marcus[41] |
| $Li^+$ | 1.98 ± 0.12 | 2.08 ± 0.07 |
| $Na^+$ | 2.34 ± 0.12 | 2.36 ± 0.06 |
| $K^+$ | 2.70 ± 0.12 | 2.80 ± 0.08 |
| $Rb^+$ | 2.94 ± 0.12 | 2.89 |
| $Cs^+$ | 3.10 ± 0.12 | 3.14 ± 0.08 |
| $Ag^+$ | 2.22 ± 0.12 | 2.42 ± 0.02 |
| $Mg^{2+}$ | 1.98 ± 0.12 | 2.09 ± 0.04 |
| $Ca^{2+}$ | 2.36 ± 0.12 | 2.42 ± 0.05 |
| $Sr^{2+}$ | 2.46 ± 0.12 | 2.64 |
| $Ba^{2+}$ | 2.70 ± 0.12 | |
| $Fe^{2+}$ | 2.10 ± 0.12 | 2.11 ± 0.01 |
| $V^{2+}$ | 2.10 ± 0.12 | |
| $Zn^{2+}$ | 1.98 ± 0.12 | 2.10 ± 0.07 |
| $Al^{3+}$ | 1.86 ± 0.12 | 1.89 ± 0.02 |
| $Ti^{3+}$ | 1.80 ± 0.12 | |
| $Fe^{3+}$ | 1.83 ± 0.12 | 2.03 ± 0.02 |
| $Cr^{3+}$ | 1.80 ± 0.12 | 1.97 ± 0.03 |

X-ray diffraction values and previous computational results compiled by Marcus.[41] These were found to have good agreement, demonstrating that the hydration shells in our simulations are structurally realistic.

In addition to the structures of the hydration shells, it is also important to ensure that these systems are behaving correctly in terms of energetics. To measure the solvation free energy of each ion, the technique of thermodynamic integration[42] was used as described by Smith et al.[43] These values are compared to experimental data from Marcus[44] in Table 2. Uncertainties are based on the statistical convergence of the free energy change during the thermodynamic integration procedure. All

**Table 2. Free Energies of Solvation of Each Metal Cation Obtained via Thermodynamic Integration at 298 K**

| | $-\Delta G_{solv}$, kcal/mol | |
|---|---|---|
| ion | this work | Marcus[44] |
| $Li^+$ | 129. ± 7.8 | 113. ± 3.1 |
| $Na^+$ | 96.3 ± 6.3 | 87.2 ± 3.1 |
| $K^+$ | 76.4 ± 2.0 | 70.5 ± 3.1 |
| $Rb^+$ | 67.9 ± 4.0 | 65.7 ± 3.1 |
| $Cs^+$ | 59.4 ± 1.3 | 59.8 ± 3.1 |
| $Ag^+$ | 105. ± 2.2 | 103. ± 3.1 |
| $Mg^{2+}$ | 471. ± 12. | 437. ± 3.8 |
| $Ca^{2+}$ | 378. ± 8.5 | 360. ± 3.8 |
| $Sr^{2+}$ | 354. ± 9.0 | 330. ± 3.8 |
| $Ba^{2+}$ | 319. ± 2.9 | 299. ± 3.8 |
| $Fe^{2+}$ | 425. ± 17. | 440. ± 3.8 |
| $V^{2+}$ | 435. ± 16. | 436. ± 6.0 |
| $Zn^{2+}$ | 477. ± 13. | 467. ± 3.8 |
| $Al^{3+}$ | 1010 ± 32. | 1080 ± 4.8 |
| $Ti^{3+}$ | 1030 ± 34. | 960. ± 7.2 |
| $Fe^{3+}$ | 1090 ± 37. | 1020 ± 4.8 |
| $Cr^{3+}$ | 1040 ± 35. | 958. ± 7.2 |

free energy data is expressed here on a scale relative to the aqueous $H^+$ ion. Again, our simulations show good agreement with the experimental results, and all calculated solvation free energies are within 10% of experimental values except for the $Li^+$ ion which presents a discrepancy of ∼13%. This is another indication that these models provide a good representation of the ions in bulk aqueous solution.

**Effective Ion Size.** When the pores are large enough, ions permeate the membrane relatively quickly in order to balance the initial concentration (chemical potential) gradient. By adjusting the LJ size parameter of the membrane atoms we can fine-tune the size of the membrane pore. A pore size that leads to no ionic permeation is defined here as the critical pore diameter, $d_c$, the largest value of $d_{pore}$ which no longer allows for the permeation of the hydrated ions. These values can be scaled by the ionic diameter based on the crystal ionic radii of Shannon[45] to produce the dimensionless relative critical pore diameter, $d_c^*$; both are shown in Table 3 (see Supporting Information for a tabulation of the Shannon radii used in scaling). The uncertainty in these measurements is defined as the standard deviation of three separate simulations for each ion. The decreasing trend of the relative critical pore diameter with increasing number of core electron shells in each group of ions correlates well with the decreasing stability of the hydration shell. Ions with high surface charge densities (such as $Li^+$, $Mg^{2+}$, and $Al^{3+}$) interact with the shell waters more strongly than they do with the membrane atoms. This means that in order for each of these ions to pass through the pore, it must be able to carry its hydration shell along with it; thereby explaining the need for a pore that is greater than ∼2.5 times the size of the bare ion.

At the other extreme, ions with low surface charge densities (such as $Cs^+$ and $Rb^+$) are not as strongly attracted to their hydration shell water molecules; their hydration shells are more likely to deform to allow for the hydrated ion to pass through the pore. For these ions, the pore size can be roughly equal to the size of the bare ion ($d_c^* \approx 1$). Figure 2 shows the effect that surface charge density has on the relative critical pore size. In this figure, the dimensionless relative critical pore size is plotted


DOI: 10.1021/acs.jced.5b00945
J. Chem. Eng. Data 2016, 61, 1578−1584

**Table 3. Critical Pore Diameter and Relative Critical Pore Diameter for Hydrated Ions, 298 K**

| ion | $d_c$, Å | $d_c^*$ |
|---|---|---|
| $Li^+$ | 4.7 ± 0.2 | 2.6 ± 0.2 |
| $Na^+$ | 4.4 ± 0.2 | 1.9 ± 0.2 |
| $Ag^+$ | 4.7 ± 0.2 | 1.8 ± 0.2 |
| $K^+$ | 4.1 ± 0.2 | 1.4 ± 0.1 |
| $Rb^+$ | 4.1 ± 0.2 | 1.2 ± 0.1 |
| $Cs^+$ | 4.0 ± 0.2 | 1.1 ± 0.1 |
| $Mg^{2+}$ | 5.8 ± 0.1 | 3.4 ± 0.2 |
| $Zn^{2+}$ | 5.7 ± 0.1 | 3.2 ± 0.2 |
| $V^{2+}$ | 5.8 ± 0.1 | 3.1 ± 0.2 |
| $Fe^{2+}$ | 5.7 ± 0.1 | 3.1 ± 0.2 |
| $Ca^{2+}$ | 6.0 ± 0.1 | 2.6 ± 0.3 |
| $Sr^{2+}$ | 6.1 ± 0.1 | 2.3 ± 0.1 |
| $Ba^{2+}$ | 6.1 ± 0.1 | 2.1 ± 0.1 |
| $Al^{3+}$ | 6.2 ± 0.1 | 4.6 ± 0.3 |
| $Fe^{3+}$ | 6.2 ± 0.1 | 4.5 ± 0.3 |
| $Cr^{3+}$ | 6.1 ± 0.1 | 4.0 ± 0.3 |
| $Ti^{3+}$ | 6.1 ± 0.1 | 3.8 ± 0.3 |

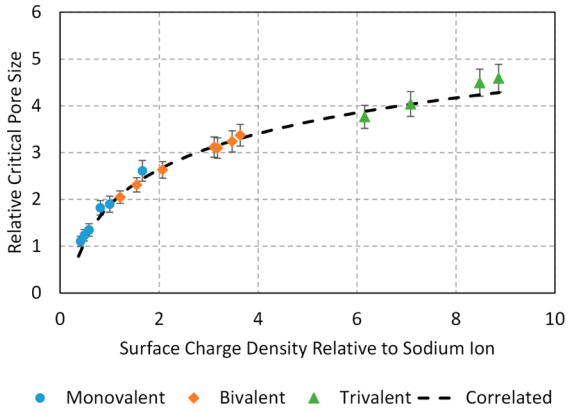


**Figure 2.** Relationship between relative critical pore size and surface charge density of various monatomic metal cations. The dashed line is the correlation presented in eq 4.

against the dimensionless relative surface charge density, defined as

$$\rho_q^* = \frac{z}{4\pi r_{ion}^2}\left(\frac{1}{\rho_{q,Na}}\right) \quad (3)$$

where $z$ is the ionic charge, $r_{ion}$ is the Shannon ionic radius in Å, and $\rho_{q,Na}$ is the surface charge density of the sodium ion. By this definition, the sodium ion has a relative surface charge density equal to unity.

As displayed in Figure 2, a clear trend exists that spans all three ionic valence families. The dotted line is mathematically described by a logarithmic relationship shown in eq 4 with the parameters fit only to the monovalent ions.

$$d_c^* = 1.1\ln(\rho_q^*) + 1.88 \quad (4)$$

This correlation for the monovalent ions seems to describe the results found for the bivalent and trivalent ions as well, suggesting that eq 4 could be used to predict the critical pore size for a wide range of cations. This predictive procedure for a molecular sieve that excludes a particular ion can thus be outlined as follows: (1) first obtain the Shannon ionic size of the ion of interest; (2) calculate the relative surface charge density of the ion using eq 3; (3) calculate the relative critical pore size using eq 4; (4) obtain the true critical pore size by multiplying the result in step 3 by the Shannon radius; (5) choose a molecular sieve that has a pore size smaller than this critical pore size. This procedure can aid in choosing the appropriate molecular sieve for removing ionic contaminants from an aqueous solution.

**Free Energy of Solvation.** This critical pore size is strongly linked to ionic charge, charge density, and free energy of solvation. A second empirical correlation was therefore sought that would enable the prediction of the free energy of solvation based on an observation of the effective ion size. Such a relationship is shown by eq 5 which correlates the solvation free energies as a function of ionic charge and the relative critical pore size.

$$\Delta G_{solv}/\Delta G_{solv,Na} = (0.4d_c^* - 0.8)(z - 0.25)^{1.5} \quad (5)$$

These are found relative to the solvation free energy of the sodium ion where $\Delta G_{solv,Na}$ is the experimental value at 298 K. Here, again, the parameters are fit to a subset of the experimental data from Marcus[44] including only a single ion from each valence level ($Li^+$, $Mg^{2+}$, and $Al^{3+}$). The expression reproduces the experimental data well, carrying an average error of ~7% as can be seen in Figure 3. This technique can be seen

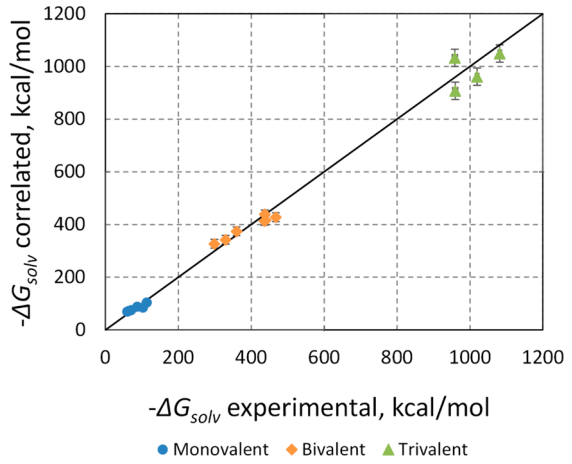


**Figure 3.** Predictions for solvation free energy from the correlation in eq 5 compared to experimental results.

as the reverse of the procedure above; here predictions are able to be made about ionic properties based on observations of whether or not ions are able to be transported through membranes containing pores of various sizes. This is similar to the correlation offered by Smith[46] in which the enthalpy of solvation was expressed as a function of ionic charge and the Pauling univalent radius.

**Effect of Temperature on Effective Ion Size.** As the effective ion size observed using this method is associated with the stability of the hydration shell, this size can be expected to decrease as the temperature increases. To examine this temperature dependence, the effective size of four ions ($Li^+$, $Cs^+$, $Mg^{2+}$, and $Ba^{2+}$) was determined using the scheme outlined previously at temperatures of 325, 350, 373, and 400 K. This particular subset of ions represents the species that have the lowest and highest charge densities among the monovalent and bivalent groups. As expected, the relative critical pore size


DOI: 10.1021/acs.jced.5b00945
J. Chem. Eng. Data 2016, 61, 1578−1584

decreases as the system temperature is increased. The relative pore size shows an Arrhenius-like behavior with inverse temperatures (Figure 4).

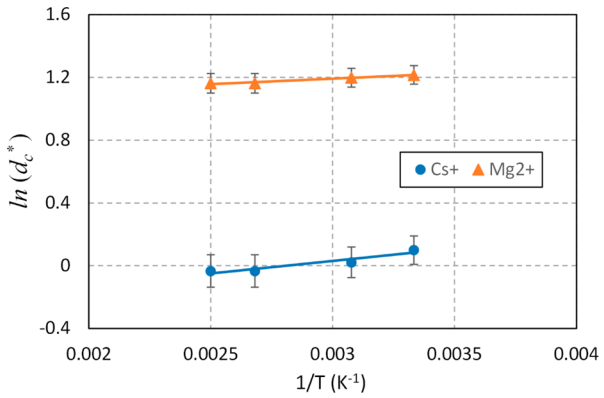


**Figure 4.** Arrhenius-type behavior of effective ion size with temperature, the slope of the line is proportional to an activation energy associated with the effective ion size change and is an indication of the thermal sensitivity.

All remaining ions were investigated at 400 K in order to test the general applicability of the behavior observed in Figure 4. The Arrhenius activation energy (which represents the dependence of the effective ionic size on temperature) was thus obtained for all the ions. Over a 100 K temperature range, we observed a ~10−12% change in $d_c^*$ for species with low relative charge densities (<1.0) and ~3% for species with high relative charge densities (>6.0) which validates the hypothesis that the variation of the effective size is strongly dependent on the stability of the hydration shell. The temperature dependence of $d_c^*$ is well represented by the equation:

$$d_c^*(T) = d_c^*(T = 298\ \mathrm{K})\ \mathrm{e}^{-E_a/RT} \quad (6)$$

The activation energies, $E_a$, associated with each ion were then compared with the free energy of solvation of that ion to determine their relationship. Figure 5 presents this dependence and as expected, there is an inverse relationship between the two (see Figure 4 which also shows this behavior). High free energies of solvation make the hydrated ions very stable, which then makes them relatively insensitive to changes in temperature. The dashed lines in Figure 5 can be described by a power law relationship:

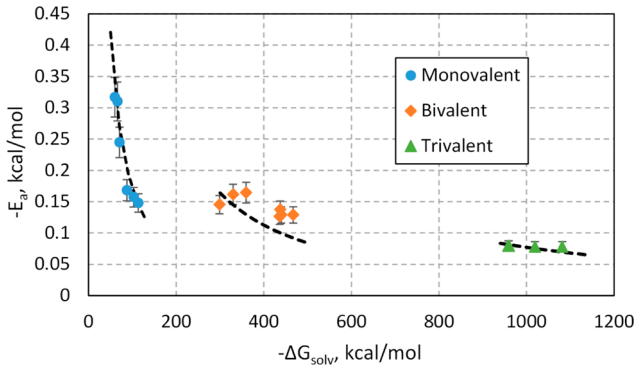


**Figure 5.** Arrhenius activation energy decreases as the solvation free energy increases due to the increased stability of the hydration shell. The dashed lines are found using the correlation presented in eq 7.

$$-E_a = 68z^2(-\Delta G_{solv})^{-1.3} \quad (7)$$

This equation (eq 7) can also be used to estimate the activation energy of other ions of interest that are not included in this study. Here, both the activation energy and the solvation free energy are expressed in units of kcal/mol.

**Effect of Temperature on Free Energy of Solvation.** Conceptually, the free energy of solvation is a measure of how much energy would be needed to completely dehydrate the ion. This value should also depend on temperature and should be of lower magnitude at elevated temperatures. To verify this trend, the thermodynamic integration method used previously was applied to the same subset of ions ($Li^+$, $Cs^+$, $Mg^{2+}$, $Ba^{2+}$) at system temperatures of 325, 350, 373, and 400 K. The correlation for $\Delta G_{solv}$ in eq 5 should also be able to capture this phenomenon due to the change in the relative critical pore size. The result of this analysis is shown for the lithium and magnesium cations in Figure 6.

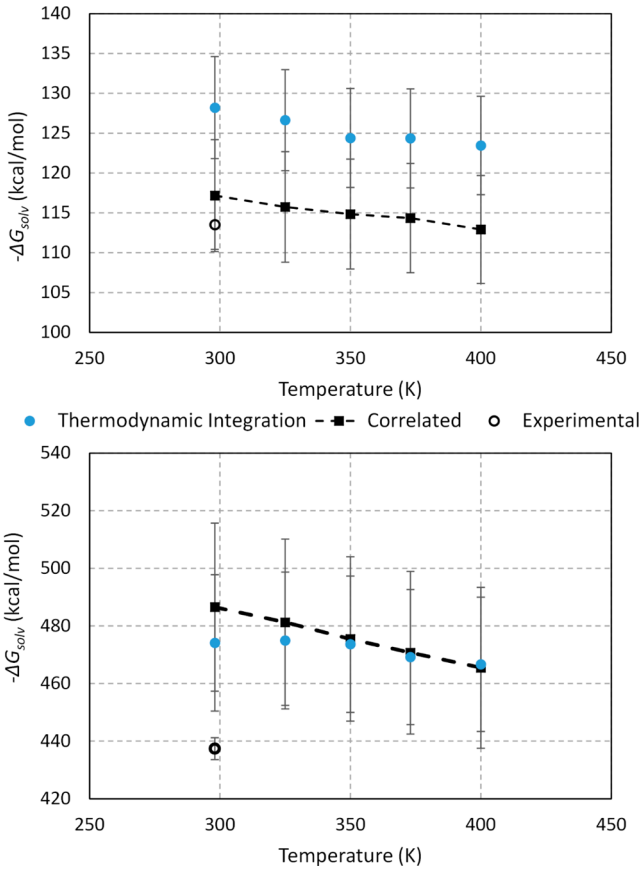


**Figure 6.** Effect of temperature on solvation free energy for $Li^+$ (top) and $Mg^{2+}$ (bottom) cations predicted using two methods: thermodynamic integration and the correlation in eq 5.

In Figure 6, both predictive methods (thermodynamic integration for the solvated ion and the general correlation found to apply to all ions) result in similar trends. While differences in the absolute values exist, they are relatively small within the scale of the error bars and may have to do with differences in the charge densities of the two ions. This indicates that the general correlation presented earlier (eq 5) can also be used to predict the free energy of solvation at different temperatures using the temperature-dependent effective ionic sizes.



DOI: 10.1021/acs.jced.5b00945
J. Chem. Eng. Data 2016, 61, 1578−1584

## CONCLUSIONS

In this study we have used nonequilibrium molecular dynamics simulations to measure the effective size of a range of cations (monovalent, bivalent, and trivalent) in aqueous solution. We observed a strong dependence between surface charge density, solvation free energy, and effective size of hydrated ions. Increasing charge density was observed to logarithmically increase the relative critical pore size due to the more stable hydration shell that results. The data from our simulations were used to develop a correlation (eq 4) that could aid in the selection of membranes for any desired separation. Conversely, if ionic transport through a porous membrane is observed, one could estimate ionic properties such as the charge density or the energy of solvation using a related empirical correlation (eq 5) we have developed. The influence of temperature on the effective size of hydrated ions was also investigated and as expected we observed that at higher temperatures the hydrated complex becomes less stable, leading to an effective decrease in the size. An Arrhenius-type relationship was used to define an activation energy for this thermally induced size change which can then also be correlated with the ion's free energy of solvation. This activation energy can be thought of as a measure of the sensitivity of the effective size to temperature fluctuations, which as expected, are more pronounced for lower solvation free energies where a small amount of thermal energy can result in a significant change in the structure of the hydration shell.

While the models used here only account for the formation of hydrated ionic complexes due to van der Waals and Coulombic forces, it is known that certain transition metals form covalent bonds with their hydration shell. While these covalent bonds may affect the residence time of water molecules in the hydration layer, the models used in this study were shown to reproduce the experimental cation−water distances even for such ions as $Fe^{3+}$ and $Cr^{3+}$; therefore, we believe our models accurately capture the structural behavior of these hydrated cation complexes as well.

## ASSOCIATED CONTENT

### Supporting Information

The Supporting Information is available free of charge on the ACS Publications website at DOI: 10.1021/acs.jced.5b00945.

Tables: Atom counts and box sizes for all monvalent, bivalent, and trivalent systems; Lennard-Jones parameters for various cations; Shannon ionic radii used to scale the effective ion sizes (PDF)

## AUTHOR INFORMATION


### Corresponding Author

*E-mail: murad@iit.edu.



### Funding

This work has been supported by a grant from the National Science Foundation (Grant No. CBET-1263707/1545560).


### Notes

The authors declare no competing financial interest.

## REFERENCES


(1) Zemaitis Jr, J. F.; Clark, D. M.; Rafal, M.; Scrivner, N. C. *Handbook of Aqueous Electrolyte Thermodynamics: Theory & Application*; John Wiley & Sons: New York, NY, 2010.

(2) Pitzer, K. S. *Activity Coefficients in Electrolyte Solutions*; CRC Press: Boca Raton, FL, 1991.

(3) Rafal, M.; Berthold, J. W.; Scrivner, N. C.; Grise, S. L. Models for Electrolyte Solutions. In Sandler, S. I., Ed.; *Models for Thermodynamic and Phase Equilibria Calculations*; Marcel Dekker: New York, NY, 1994; p 601.

(4) Loehe, J. R.; Donohue, M. D. Recent Advances in Modeling Thermodynamic Properties of Aqueous Strong Electrolyte Systems. *AIChE J.* **1997**, *43*, 180−195.

(5) Anderko, A.; Wang, P.; Rafal, M. Electrolyte Solutions: From Thermodynamic and Transport Property Models to the Simulation of Industrial Processes. *Fluid Phase Equilib.* **2002**, *194*, 123−142.

(6) Chen, C.-C.; Mathias, P. M.; Orbey, H. Use of Hydration and Dissociation Chemistries with the electrolyte−NRTL Model. *AIChE J.* **1999**, *45*, 1576−1586.

(7) Paritosh, F.; Murad, S. Molecular Simulations of Osmosis and Reverse Osmosis in Aqueous Electrolyte Solutions. *AIChE J.* **1996**, *42*, 2984−2986.

(8) Koros, W. J.; Fleming, G. K. Membrane-Based Gas Separation. *J. Membr. Sci.* **1993**, *83*, 1−80.

(9) Pandey, P.; Chauhan, R. S. Membranes for Gas Separation. *Prog. Polym. Sci.* **2001**, *26*, 853−893.

(10) Qiu, M. M.; Hwang, S.-T. Continuous Vapor-Gas Separation with a Porous Membrane Permeation System. *J. Membr. Sci.* **1991**, *59*, 53−72.

(11) Scholes, C. A.; Stevens, G. W.; Kentish, S. E. Membrane Gas Separation Applications in Natural Gas Processing. *Fuel* **2012**, *96*, 15−28.

(12) Loeb, S.; Sourirajan, S. High Flow Porous Membranes for Separating Water from Saline Solutions. U.S. Patent US3133132 A, May 12, 1964.

(13) Kesting, R. E. Semipermeable Membranes of Cellulose Acetate for Desalination in the Process of Reverse Osmosis. I. Lyotropic Swelling of Secondary Cellulose Acetate. *J. Appl. Polym. Sci.* **1965**, *9*, 663−688.

(14) Manjikian, S. Desalination Membranes from Organic Casting Solutions. *Ind. Eng. Chem. Prod. Res. Dev.* **1967**, *6*, 23−32.

(15) McCutcheon, J. R.; McGinnis, R. L.; Elimelech, M. A Novel Ammonia—carbon Dioxide Forward (direct) Osmosis Desalination Process. *Desalination* **2005**, *174*, 1−11.

(16) Huckins, J. N.; Manuweera, G. K.; Petty, J. D.; Mackay, D.; Lebo, J. A. Lipid-Containing Semipermeable Membrane Devices for Monitoring Organic Contaminants in Water. *Environ. Sci. Technol.* **1993**, *27*, 2489−2496.

(17) Meadows, J.; Tillitt, D.; Huckins, J.; Schroeder, D. Large-Scale Dialysis of Sample Lipids Using a Semipermeable Membrane Device. *Chemosphere* **1993**, *26*, 1993.

(18) Strandberg, B.; Bergqvist, P.-A.; Rappe, C. Dialysis with Semipermeable Membranes as an Efficient Lipid Removal Method in the Analysis of Bioaccumulative Chemicals. *Anal. Chem.* **1998**, *70*, 526−533.

(19) La Mantia, F.; Pasta, M.; Deshazer, H. D.; Logan, B. E.; Cui, Y. Batteries for Efficient Energy Extraction from a Water Salinity Difference. *Nano Lett.* **2011**, *11*, 1810−1813.

(20) Schwenzer, B.; Zhang, J.; Kim, S.; Li, L.; Liu, J.; Yang, Z. Membrane Development for Vanadium Redox Flow Batteries. *ChemSusChem* **2011**, *4*, 1388−1406.

(21) Prifti, H.; Parasuraman, A.; Winardi, S.; Lim, T. M.; Skyllas-Kazacos, M. Membranes for Redox Flow Battery Applications. *Membranes* **2012**, *2*, 275−306.

(22) Moser, I.; Jobst, G.; Urban, G. A. Biosensor Arrays for Simultaneous Measurement of Glucose, Lactate, Glutamate, and Glutamine. *Biosens. Bioelectron.* **2002**, *17*, 297−302.

(23) Santus, G.; Baker, R. W. Osmotic Drug Delivery: A Review of the Patent Literature. *J. Controlled Release* **1995**, *35*, 1−21.

(24) Lavan, D. A.; McGuire, T.; Langer, R. Small-Scale Systems for in Vivo Drug Delivery. *Nat. Biotechnol.* **2003**, *21*, 1184−1191.

(25) Makhija, S. N.; Vavia, P. R. Controlled Porosity Osmotic Pump-Based Controlled Release Systems of Pseudoephedrine: I. Cellulose Acetate as a Semipermeable Membrane. *J. Controlled Release* **2003**, *89*, 5−18.




DOI: 10.1021/acs.jced.5b00945
*J. Chem. Eng. Data* 2016, 61, 1578−1584

(26) Liu, H.; Jameson, C. J.; Murad, S. Molecular Dynamics Simulation of Ion Selectivity Process in Nanopores. *Mol. Simul.* **2008**, *34*, 169−175.
(27) Hinkle, K. R.; Jameson, C. J.; Murad, S. Transport of Vanadium and Oxovanadium Ions Across Zeolite Membranes: A Molecular Dynamics Study. *J. Phys. Chem. C* **2014**, *118*, 23803−23810.
(28) Malani, A.; Ayappa, K. G.; Murad, S. Effect of Confinement on the Hydration and Solubility of NaCl in Water. *Chem. Phys. Lett.* **2006**, *431* (1−3), 88−93.
(29) Laliberté, M.; Cooper, W. E. Model for Calculating the Density of Aqueous Electrolyte Solutions. *J. Chem. Eng. Data* **2004**, *49*, 1141−1151.
(30) Berendsen, H. J. C.; Grigera, J. R.; Straatsma, T. P. The Missing Term in Effective Pair Potentials. *J. Phys. Chem.* **1987**, *91*, 6269−6271.
(31) Joung, I. S.; Cheatham, T. E. Determination of Alkali and Halide Monovalent Ion Parameters for Use in Explicitly Solvated Biomolecular Simulations. *J. Phys. Chem. B* **2008**, *112*, 9020−9041.
(32) Mamatkulov, S.; Fyta, M.; Netz, R. R. Force Fields for Divalent Cations Based on Single-Ion and Ion-Pair Properties. *J. Chem. Phys.* **2013**, *138*, 024505.
(33) Dubois, V.; Seijo, M.; Archirel, P. On the Absorption Spectrum and Stability of Ag32+ in Aqueous Solution. *Chem. Phys. Lett.* **2004**, *389*, 150−154.
(34) Aguilar, C. M.; De Almeida, W. B.; Rocha, W. R. The Electronic Spectrum of Fe2+ Ion in Aqueous Solution: A Sequential Monte Carlo/quantum Mechanical Study. *Chem. Phys. Lett.* **2007**, *449*, 144−148.
(35) Ansari, A.; Mehrabian, M. A.; Hashemipour, H. Zinc Ion Adsorption on Carbon Nanotubes in an Aqueous Solution. *Pol. J. Chem. Technol.* **2012**, *14*, 29−37.
(36) Li, P.; Roberts, B. P.; Chakravorty, D. K.; Merz, K. M. Rational Design of Particle Mesh Ewald Compatible Lennard-Jones Parameters for + 2 Metal Cations in Explicit Solvent. *J. Chem. Theory Comput.* **2013**, *9*, 2733−2748.
(37) Faro, T. M. C.; Thim, G. P.; Skaf, M. S. A Lennard-Jones plus Coulomb Potential for Al3+ Ions in Aqueous Solutions. *J. Chem. Phys.* **2010**, *132*, 114509.
(38) Won, Y. Force Field for Monovalent, Divalent, and Trivalent Cations Developed under the Solvent Boundary Potential. *J. Phys. Chem. A* **2012**, *116*, 11763−11767.
(39) Martínez, L.; Andrade, R.; Birgin, E. G.; Martínez, J. M. PACKMOL: A Package for Building Initial Configurations for Molecular Dynamics Simulations. *J. Comput. Chem.* **2009**, *30*, 2157−2164.
(40) Plimpton, S. Fast Parallel Algorithms for Short-Range Molecular Dynamics. *J. Comput. Phys.* **1995**, *117*, 1−19.
(41) Marcus, Y. Ionic Radii in Aqueous Solutions. *Chem. Rev.* **1988**, *88*, 1475−1498.
(42) Frenkel, D.; Smit, B. *Understanding Molecular Simulation: From Algorithms to Applications*; Academic Press: San Diego, CA, 2001.
(43) Smith, E. J.; Bryk, T.; Haymet, A. D. J. Free Energy of Solvation of Simple Ions: Molecular-Dynamics Study of Solvation of Cl− and Na+ in the Ice/water Interface. *J. Chem. Phys.* **2005**, *123*, 034706.
(44) Marcus, Y. Thermodynamics of Solvation of Ions. Part 5. Gibbs Free Energy of Hydration at 298.15 K. *J. Chem. Soc., Faraday Trans.* **1991**, *87*, 2995−2999.
(45) Shannon, R. D. Revised Effective Ionic Radii and Systematic Studies of Interatomic Distances in Halides and Chalcogenides. *Acta Crystallogr., Sect. A: Cryst. Phys., Diffr., Theor. Gen. Crystallogr.* **1976**, *32*, 751−767.
(46) Smith, D. W. Ionic Hydration Enthalpies. *J. Chem. Educ.* **1977**, *54*, 540−542.


DOI: 10.1021/acs.jced.5b00945
*J. Chem. Eng. Data* 2016, 61, 1578−1584